THE ASTROPHYSICAL JOURNAL, 536:380–392, 2000 June 10

THERMALLY DOMINATED CARBON MONOXIDE EMISSION IN THE TAURUS MOLECULAR CLOUD COMPLEX

E. F. LADD
Department of Physics, Bucknell University, Lewisburg, PA 17837
AND
K. R. COVEY
Department of Physics, Carleton College, Northfield, MN 55057
Received 1999 October 19; accepted 2000 January 14

ABSTRACT

We analyze the structure of a region of the Taurus molecular cloud containing star-forming dense cores, as traced by emission from the $J = 1$–0 rotational transition of the carbon monoxide isotopomer, $C^{18}O$. While the spatial structure of the velocity-integrated emission is rather featureless, there is substantial structure in the emission integrated over small velocity widths, and the entire three-dimensional data set (right ascension, declination, and velocity) can be broken into a collection of nearly discrete components. We construct a cloud model consisting of nine individual Gaussian components and find that the data are best replicated when these components have sizes of ~ 0.1 pc and velocity dispersions comparable to or smaller than the thermal velocity dispersion of molecular hydrogen at a temperature of 10 K. We find that nearly all of the molecular mass of the cloud is contained within these quiescent structures. At least two of the structures are detected in observations in the $J = 4$–3 line of HC_3N; these two structures are likely associated with the two forming stars in the region. Our results suggest that thermally dominated structures may be common in regions containing dense cores, but that many of these structures are insufficiently dense to be detected with dense gas tracers.

Subject headings: ISM: clouds — ISM: individual (Taurus Molecular Cloud) — ISM: molecules — radio lines: ISM

1. INTRODUCTION

The structure and dynamics of molecular clouds remain poorly understood despite decades of intense study. The principal difficulty preventing better understanding is the simple fact that observers have direct access to only three of the six dimensions of the phase space that these clouds occupy. The distribution of material along the line of sight is not an observable quantity and only in exceptional cases can the velocity of cloud material in the plane of the sky be inferred. To make matters worse, observations of the same region with different tracers often show substantially different structure. Variations in chemistry, different levels of excitation, and radiative transfer effects make the comparison of data from different tracers difficult.

Observations in the low-energy rotational transitions of carbon monoxide have often been used as tracers of cloud material. CO has a relatively stable abundance over a relatively wide range of physical conditions within clouds (Bergin & Langer 1997), and the correspondence between visual extinction and CO emission is well established (Frerking, Langer, & Wilson 1982; Lada et al. 1994). Its low dipole moment (0.11 D) ensures that it will be excited (and often thermalized) throughout most of a typical cold molecular cloud. Because of the high abundance and low dipole moment of CO, the rotational lines often have high optical depth, and so CO observations are less sensitive to material deep within cloud cores. However, the emission lines from the less abundant isotopomers of CO, particularly $C^{18}O$, have substantially lower optical depth and can faithfully trace structure throughout the cloud.

Thus $C^{18}O$ observations *should* be sensitive to all of the material within a molecular cloud, including the dense cores out of which stars form. In practice, however, $C^{18}O$ mapping reveals structures much larger and more turbulent than the typical star forming dense core. Typical $C^{18}O$ cores have sizes of 0.2 pc or larger, full width at half-maximum (FWHM) line widths of 1.0 km s^{-1}, and masses of $\sim 10\ M_\odot$ (e.g., Onishi et al. 1996). Only when observations are made in the lines of molecules with higher dipole moments (which therefore require higher densities for excitation) such as NH_3 and HC_3N do the smaller, more quiescent dense cores become readily visible. These structures are typically smaller, with sizes of 0.1 pc or less, have much narrower FWHM line widths, and have masses of $\sim 1\ M_\odot$ (e.g., Benson & Myers 1989).

Reconciling these two views of the same region has often involved the invocation of a two-component model: a turbulent, "fluffy" outer portion of the cloud, where gas densities are lower and motions are largely supersonic, and a dense inner region, where the material is dominated by thermal motions (e.g., Goodman et al. 1998). Within this paradigm, the broad line width $C^{18}O$ observations are dominated by emission from the outer region, while only the tracers of high-density material "see" the inner dense core.

Even if this picture is largely correct, the dense core also emits in $C^{18}O$, and based on its relatively large mass and narrow line width, $C^{18}O$ spectra should contain evidence of its presence. In this paper, we present the results of a search for this signature in $C^{18}O$ emission toward one star-forming region in the Taurus molecular cloud. We examine both the position and velocity information contained within our observations simultaneously and find that we can identify the quiescent dense cores responsible for star formation. We confirm this identification with observations of dense gas in the $J = 4$–3 line of HC_3N, showing that the line

center velocities and line widths measured in the dense gas tracer correspond to components of the $C^{18}O$ data cube.

Moreover, we find that most, if not all, of the observed $C^{18}O$ emission arises from thermally dominated clumps that are resolved in the spatial and velocity dimensions and are largely distinct within our data cube. We conclude that the large line width and spatial extent typical of $C^{18}O$ cores in star-forming region may result from the superposition of a number of thermally dominated clumps whose size, line width, and mass are comparable to those of dense star-forming cores.

1.1. *The I04181 Region*

We have chosen to study a region of recent star formation in the Taurus molecular cloud, which we label the "I04181" region after the first portion of the *IRAS* designation for the cloud's infrared sources. This region is located along the filament of dense gas extending southeastward from the L1495 complex (Lynds 1962) and containing the knots labeled B213, B216, B217, and B218 by Barnard (1927). Visual star counts using a 4.5 cell indicate an average extinction of 6 magnitudes toward the region (Gaida, Ungerechts, & Winnewisser 1984). We adopt a distance of 145 pc, which is a compromise between the distance based on spectroscopic parallaxes of field stars near Taurus (Kenyon, Dobrzycka, & Hartmann 1994; 140 ± 10 pc) and a statistically derived distance based on the rotation properties of T Tauri stars associated with the cloud (Preibisch & Smith 1997; 152 ± 10).

The region contains two far-infrared sources identified by the *IRAS* Point Source Catalog, while three near-infrared sources have been detected by Kenyon et al. (1993). All three sources have steep near-infrared colors, suggesting that they are deeply embedded within the cloud material and therefore quite young. Dense gas has been detected toward the northern source (IRAS 04181+2655) by Hogerheijde et al. (1997) and Moriarty-Schieven et al. (1995), and $C^{18}O$ $J = 1$–0 mapping of the region immediately surrounding the northern source is presented by Juvela et al. (1997).

This region was chosen for study because of the presence of several forming stars in close proximity and because of the remarkable velocity structure in the $C^{18}O$ spectra (see below). These observations are part of a larger survey of many dense core regions in the Taurus molecular cloud.

1.2. *Organization of This Work*

We present observations in the $J = 1$–0 line of $C^{18}O$ and the $J = 4$–3 line of HC_3N in § 2. In § 3 we discuss our method for decomposing the $C^{18}O$ data cube and identifying individual structures within the cloud. We also discuss the properties of these structures and their correspondence with the dense gas and forming stars in this section. In § 4 we discuss the stability of these structures and the implications for our understanding of cloud structure in regions containing dense cores. We present our conclusions in § 5.

2. OBSERVATIONS

2.1. $C^{18}O$ $J = 1$–0 *Observations*

We observed the $J = 1$–0 rotational transition of $C^{18}O$ (109.782156 GHz) toward the I04181 region with the 14 m telescope of the Five College Radio Astronomy Observatory (FCRAO)[1] in 1995. The $C^{18}O$ data were obtained on 1995 February 8 and March 2. We observed a $250'' \times 300''$ (0.18×0.21 pc) region with $25''$ sampling.

The data were obtained with the FCRAO 15 beam QUARRY receiver array (Erickson et al. 1992) and the 1024 channel FAAS autocorrelator, with channel spacing of 19.5 kHz, which with uniform weighting produced a full width at half-maximum (FWHM) velocity resolution of 0.06 km s^{-1}. The pointing of the telescope was checked and updated with observations of the strong stellar SiO maser IK Tau at the beginning and end of each observing session. Pointing corrections were less than $7''$ in azimuth and elevation. All observations were calibrated by a chopper wheel technique that allowed switching between the sky and an ambient temperature load. Data were obtained by frequency switching, with an offset frequency of 4 MHz (10.95 km s^{-1}). System temperatures were 470–500 K for the $C^{18}O$ observations and 630–700 K for the $C^{17}O$ observations. The total on-source integration time was 30 minutes per position in $C^{18}O$ and 131 minutes per position in $C^{17}O$ yielding rms noise levels of 0.12 and 0.09 K, respectively. The half-power beamwidth ($\Theta_B = 48''$) was determined from observations of Mars, and the forward scattering and spillover efficiency ($\eta_{\rm fss} = 0.72$) was determined from observations of the Moon. The locations of each observation are depicted in Figure 1, which plots the $C^{18}O$ integrated intensity.

The $C^{18}O$ data were converted to a radiation temperature (T_R^*) scale by dividing the antenna temperature (T_A^*) scale output from the chopper wheel calibration by $\eta_{\rm fss}$ (Kutner & Ulich 1981). This temperature scale was chosen over a main-beam brightness temperature ($T_{\rm mb}$) scale for two related reasons: first, the $C^{18}O$ emission in this region is extended over angular sizes significantly larger than the FWHM beam size of the observations (see Figs. 1 and 3), and second, the error beam of the FCRAO 14 m telescope is largely confined to angular scales of $\sim 100''$ or smaller (Ladd & Heyer 1996).[2]

2.2. HC_3N $J = 4$–3 *Observations*

Several positions in the same region were observed in the $J = 4$–3 transition of HC_3N (36.392324 GHz) with the NEROC Haystack Observatory[3] during an observing session in 1998 July 13 and 14. The data were obtained with the facility dual-channel receiver system, which allowed for simultaneous observations of both polarizations. The data were fed to the facility autocorrelator spectrometer, which produced spectra containing 8192 channels with 241 Hz (0.002 km s^{-1}) spacing for both polarizations.

Typical system temperatures were 150–200 K for the better of the two receiver channels, while the second channel often had system temperatures ~ 30–50 K higher. The pointing of the telescope was monitored with observations of the planets Venus and Jupiter; typical pointing

[1] The Five College Radio Astronomy Observatory is operated with support from the National Science Foundation under grant AST 94-20159 and with permission of the Metropolitan District Commission of Massachusetts.

[2] There also exists a poorly measured but likely small error beam component at large angles ($\sim 2°$) owing to the space frame of the observatory's radome.

[3] Undergraduate research at the Haystack Observatory of the Northeast Radio Observatory Corporation (NEROC) is supported by a grant from the National Science Foundation.

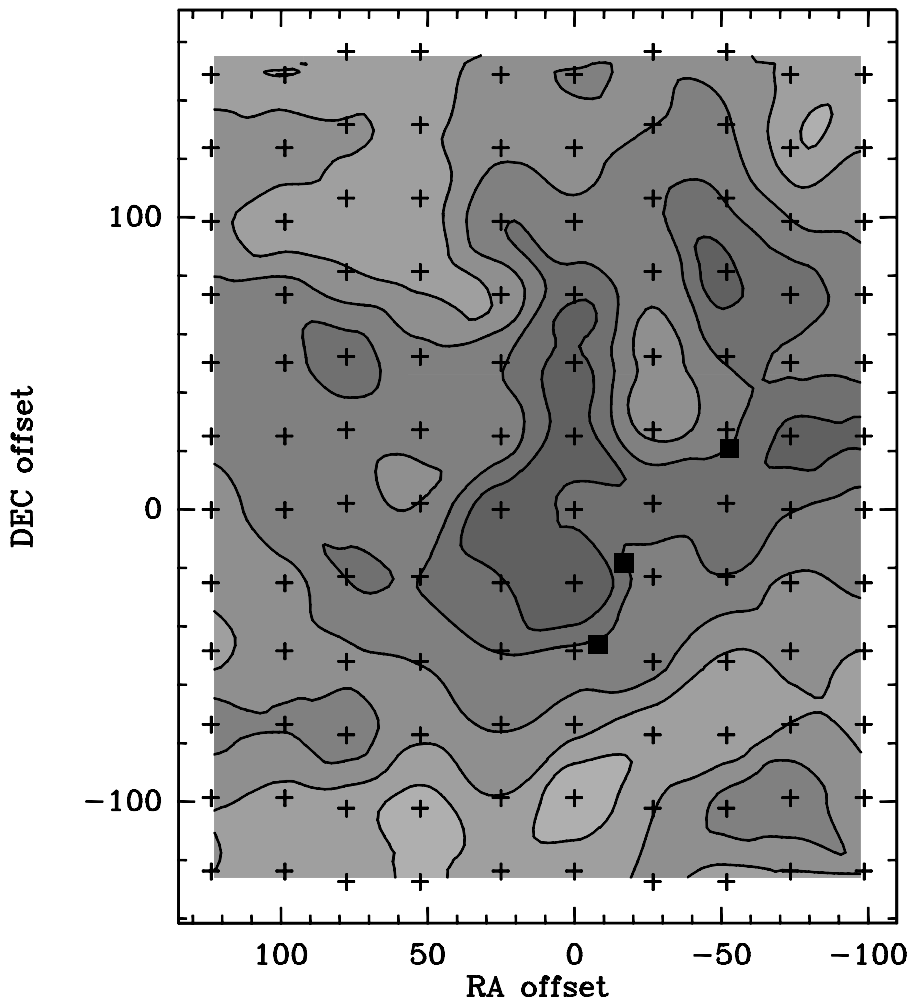

FIG. 1.—$C^{18}O$ $J = 1$–0 integrated intensity ($\int_4^8 T_R^* dv$) toward the I04181 region in Taurus, taken with the FCRAO 14 m telescope. Coordinates indicate offset in arcseconds from the (0, 0) position of $04^h18^m 6^s.9$, 26°54′54″ (1950). Contours begin at 0.8 K km s^{-1} and increment by 0.15 K km s^{-1}. The positions observed are marked with plus signs, and the positions of the three infrared sources with steep spectral slopes found by Kenyon et al. (1993) are indicated by filled squares.

offsets were 7″ in both azimuth and elevation. The half-power beamwidth ($\Theta_B = 64''$) and aperture efficiency ($\eta_A = 0.36$) were determined from drift-scan maps of Venus.

In this paper, we use only the line center velocity and line width information from the HC_3N data (see § 3.4), so we have chosen to present these data on an antenna temperature (T_A^*) scale. The HC_3N emission is likely less extended than the $C^{18}O$ emission, so conversion to a radiation temperature (T_R^*) scale is probably inappropriate. Calibration to a more physically meaningful intensity scale must await a better sampled map which delineates the angular distribution of the emission.

3. RESULTS

The $C^{18}O$ integrated intensity map is shown in Figure 1, along with the locations of three infrared sources found by Kenyon et al. (1993). Throughout the mapped region, the total intensity varies by less than a factor of 2. There are two local maxima in integrated intensity—one located ~60″ north of the northern near-infrared source, and another brighter maximum ~30″ northeast of the southern source. However, neither is defined at the half-power contour within the mapped area. We calculate the column density at each position in our map, assuming that the emission is thermalized with an excitation temperature of 10 K. We convert these $C^{18}O$ column densities to H_2 column densities using the conversion of Frerking et al. (1982). The derived H_2 column densities range from 5 to 9×10^{21} cm^{-2}, with an average column density of 6.5×10^{21} cm^{-2}. We measure a total mass of 4.2 $M_\odot$ within the mapped area. For excitation temperatures ranging from 6 to 12 K, the calculated mass varies by less than 10%.

3.1. *Velocity-resolved Structure*

While the integrated intensity map shows little variation with position, a wealth of structure is evident from the velocity-resolved images. The spectra toward this region are not at all similar to one another and show that the cloud material is divided into several components distinct in velocity. The observed spectra are shown in a grid format in Figure 2. A large number of spectra are multiple-peaked and toward several positions, particularly in the northeast, three or more velocity components can be identified.

While the spectra change radically in shape from one side of the map to the other, adjacent spectra appear much less

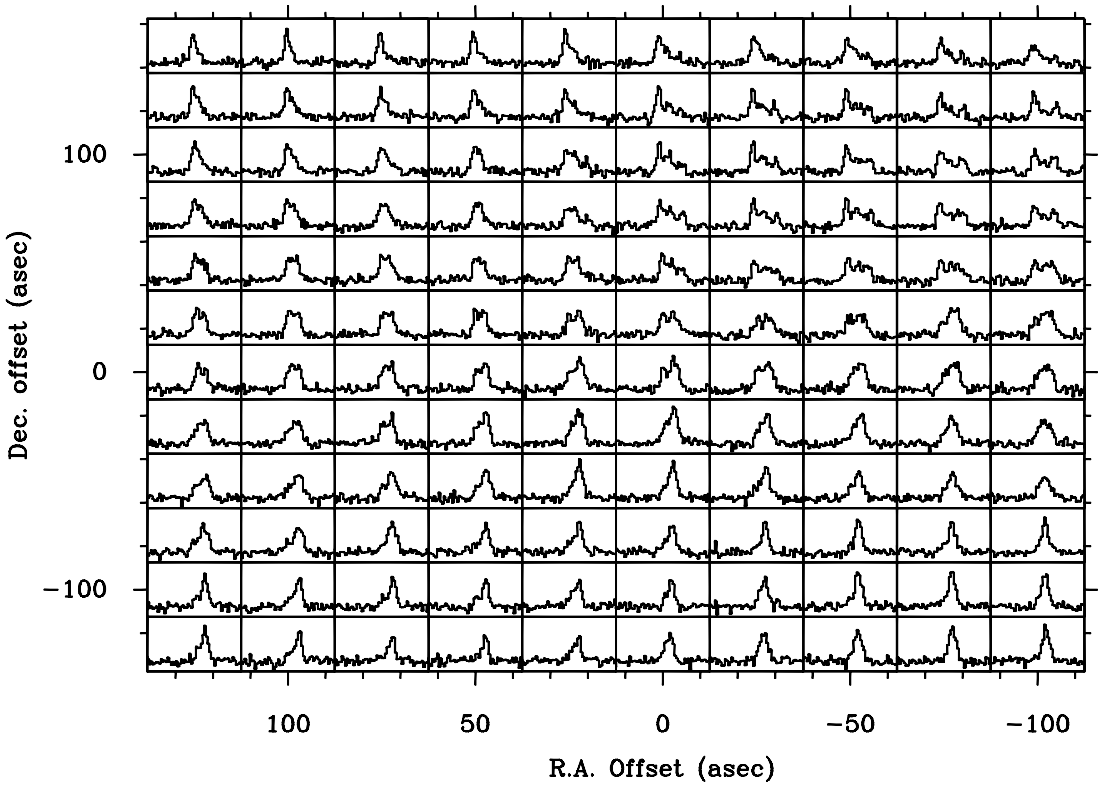

FIG. 2.—$C^{18}O$ $J = 1$–0 spectra toward 120 positions in the I04181 region in Taurus, taken with the FCRAO 14 m telescope. Coordinates indicate offset in arcseconds from the (0, 0) position of $04^h18^m6\overset{s}{.}9$, 26° 54′54″ (1950). For each spectrum, the x-axis represents LSR velocity and ranges from 3 to 9 km s^{-1}, and the y-axis represents T_R^* and ranges from −0.5 to 2.2 K.

different from one another. This effect occurs partly because the data are densely sampled, i.e., the angular separation between observations (25″) is less than the FWHM beam size (48″), but also because the various velocity components are larger in angular size than the beam. For example, a single component can be traced in the column of right ascension offset = 0 spectra from the bottom of the mapped area well past the middle of the map. To the north of the (0,0) position, however, that component disappears and is replaced by another structure at lower LSR velocity. In fact, the complicated velocity structure in all of the spectra can be understood as arising from varying contributions from a small number of spatially extended velocity components.

The channel maps shown in Figure 3 demonstrate the spatial structure of each of the velocity components. Note that emission with $V_{LSR} \sim 5.8$ km s^{-1} is largely confined to the northern part of the mapped area and is spatially distinct from a clump of emission with $V_{LSR} \sim 6.6$ km s^{-1} farther to the south. In general, the emission appears to be concentrated into somewhat distinct, but overlapping, knots of emission in our data cube.

The wealth of velocity structure in our maps indicates that the column density derived from velocity-integrated intensities gives a very incomplete description of the distribution of material in this region. Therefore, we recalculate the $C^{18}O$ column density at each position *and velocity*, creating a three-dimensional cube of $C^{18}O$ *spectral column density* with units of cm^{-2} $(km\ s^{-1})^{-1}$. We use the same assumptions employed above for the integrated intensities to derive $C^{18}O$ spectral column densities, that is, we determine the optical depth of 10 K $C^{18}O$ required to produce the emission observed at each voxel.[4] The derived optical depth and the velocity width of each voxel then gives a spectral column density at each position.

Throughout most of the data cube, this operation results in a linear scaling of the intensity in each voxel into a spectral column density, but at locations with high intensities, the derived spectral column densities are considerably higher than those implied by a linear scaling because of optical depth effects. Voxels of high intensity are found to have substantial optical depth ($\tau > 1$) for an excitation temperature of 10 K, and the spectral column densities implied are higher to account for the saturated emission. The resulting spectral column density data cube looks much like the original data cube, except that its dynamic range is greater, and peaks are more pronounced.[5] Figure 4 shows the effect of this mapping from intensity to column density for one representative spectrum.

[4] A voxel denotes a location and surrounding small volume in a three-dimensional cube, just as a pixel denotes a location and surrounding small area in a two-dimensional image.

[5] In performing this process, we are trading one assumption, that all of the $C^{18}O$ emission is optically thin, for another assumption, that all of the emission has an excitation temperature of 10 K. For all of the emission to be optically thin, the excitation temperatures would have to be substantially greater than the kinetic temperatures typically observed in Taurus, so we reject that assumption. However, it must be noted that the excitation temperature might vary over the mapped region, especially in regions of low intensity where the $C^{18}O$ might not be fully thermalized. Luckily, the relationship between intensity and spectral column density is not strongly dependent on excitation temperature in this temperature regime, as was noted previously for integrated intensity and column density.

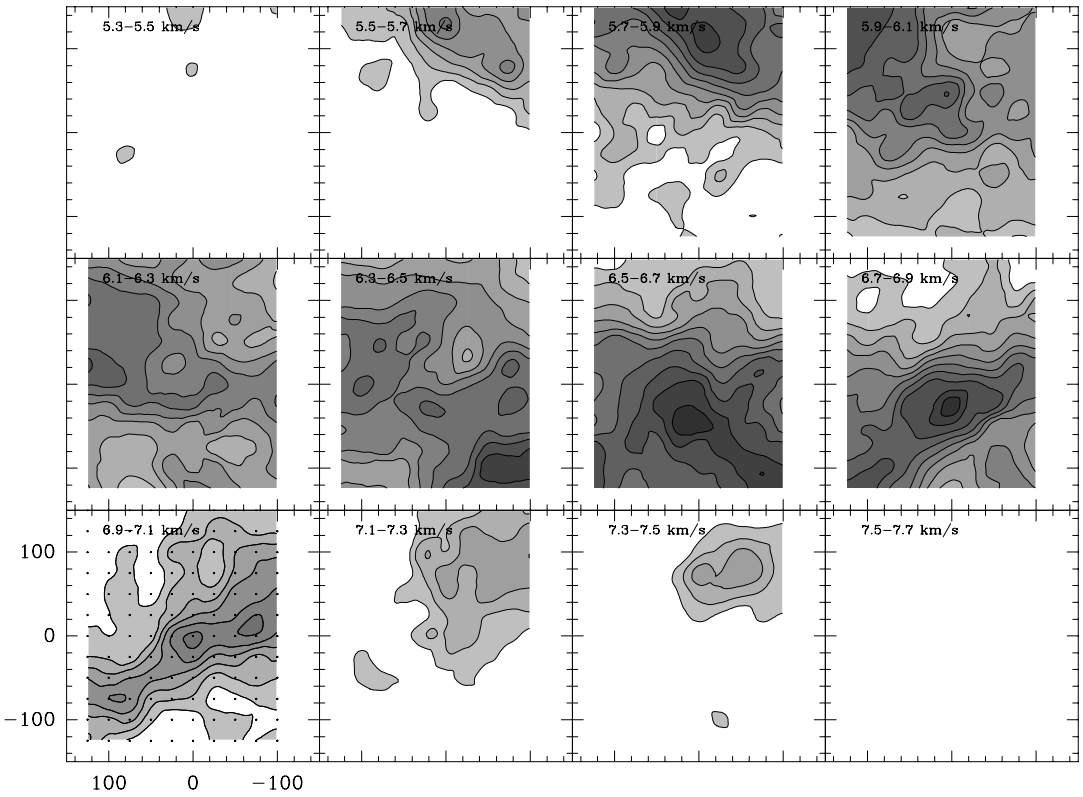

FIG. 3.—Maps of $C^{18}O$ radiation temperature (T_R^*) integrated over 0.2 km s^{-1} intervals from $V_{LSR} = 5.3$ to 7.7 km s^{-1}. Contour levels begin at 0.04 K km s^{-1} and increment by 0.03 K km s^{-1}. Coordinates on the lower left-hand panel indicate offset in arcseconds from the (0, 0) position of $04^h18^m6.9^s$, 26°54′54″ (1950) and apply for all panels.

The peak value in the spectral column density cube is 1.8×10^{15} cm^{-2} (km s^{-1})$^{-1}$, and the rms "noise" level, determined from examination of voxels at high and low velocities where no cloud emission is likely, is 1.3×10^{14} cm^{-2} (km s^{-1})$^{-1}$.

3.2. *Cube Decomposition*

Motivated by the appearance of the spectra and channel maps, we attempted to model the observed emission as a collection of structures with Gaussian shapes in both position and velocity. Each component was defined by eight properties—its peak spectral column density, its location within the cube (two space coordinates and one velocity coordinate), the FWHM size of the major and minor axes in the spatial plane, the position angle of the major axis in the spatial plane, and its FWHM size in velocity. Thus these components are allowed to have elliptical Gaussian shapes, but only a static velocity structure (i.e., no shear or rotation).

We chose Gaussians for our model for several reasons. First, when single velocity components could be identified in the observed spectra, they appeared to have Gaussian line shapes. Second, the underlying cloud structure has already been smoothed by the (nearly) Gaussian beam of the 14 m telescope. Last, Gaussian structures can be defined rather simply with a relatively small number of free parameters.

Initial guesses for each parameter for each of the individual structural components were obtained from visual examination of the spectral column density cube. We attempted to create a model cube with a minimum number of structures, so we proceeded iteratively. We first identified several prominent structures in the channel maps and created a model cube using only these structures. We then differenced the model and spectral column density cubes and determined if additional components were needed. Using this procedure, we constructed a model of the spectral column density cube using nine individual components.

Because each component is defined by eight properties, our resulting model contained 72 free parameters for a cube of nearly 5000 (mostly) independent measurements. The reduced χ^2 for our model with the parameters judged by eye from examination of the spectral column density cube was 9.2.

From this starting point, we embarked on a χ^2 minimization process to determine the best-fit set of parameters. We used a "differential evolution" algorithm described by Price & Storn (1997) to search the large χ^2 space. This algorithm is well suited to searches of complicated and multidimensional χ^2 spaces and is not easily fooled by the many local minima found in such domains.

The technique involves the creation of a large initial set of potential solutions (the "parent" set), which are then combined to produce a set of new solutions (the "child" set). Solutions in the child set contain attributes from several different parents. The parents and children then compete for survival based on their goodness of fit to the spectral column density cube, and the survivors then produce new offspring. An additional feature is the introduction of random variation in each of the parameters ("mutation" in

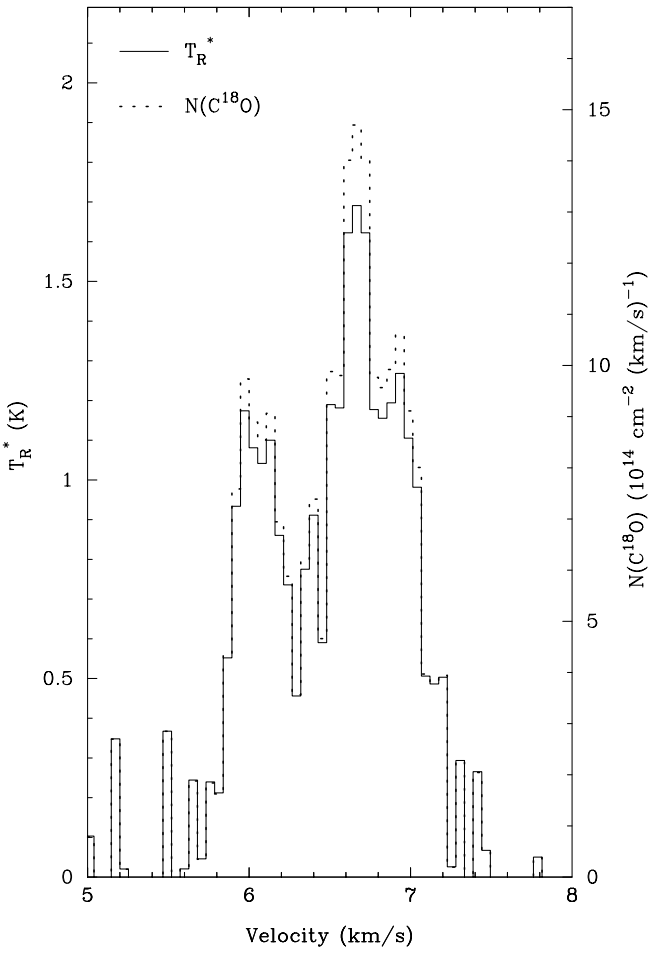

FIG. 4.—Comparison between radiation temperature (T_R^*; *solid lines*) and derived spectral column density (*dashed lines*) as a function of velocity for emission toward the (0, 0) position. The temperature scale is plotted on the vertical axis at left, while the spectral column density scale is plotted on the vertical axis at right. At velocities where the dashed line does not appear, the solid and dashed lines are coincident.

the biological analog), thereby allowing for a sparse search of the parameter space to test the stability of the current set of solutions.

As with biological evolution, the success of this parameter set natural selection process depends on tracking a large population through many generations. In our minimization, we followed 2600 generations of a population of 315 solutions. During this process, the model was modified such that the χ^2 of the best-fit set of parameters was reduced to 1.55.[6]

We subsequently searched around this best-fit location in the χ^2 space to determine the sensitivity of the χ^2 to variations in each parameter. We assign a 1 σ uncertainty to each parameter, the value of which is set by the change in that parameter which results in a increase in the χ^2 by one.[7]

Channel maps of the data, our best-fit model, and the residuals are shown in Figure 5 for two representative narrow velocity ranges, and a comparison between a representative spectrum and the model result is shown in Figure 6. These figures show qualitatively the extent to which the model replicates the structure within the data cube. The channel maps in Figure 5 show that the spatial distribution of emission is generally a bit more centrally peaked than the model fit; this result suggests that, for at least a few of the clumps, a function with a more pronounced central emission peak, such as a power law, might result in a better fit.

3.3. *Clump Properties*

The best-fit parameters for our nine Gaussian component model are shown in Table 1. For each parameter, the 1 σ uncertainty is indicated in parentheses. All of the clumps have peaks greater than or equal to 6.6×10^{14} cm^{-2} (km s^{-1})$^{-1}$, or 5 times the rms noise level in the spectral column density cube. Clump FWHM sizes and line widths are also significantly greater than the resolutions of the observations. Last, all clumps have line center velocities in the

[6] This method of cloud decomposition differs from existing clump identification routines in several ways. Unlike the CLUMPFIND algorithm developed by Williams et al. (1994), our method allows for the distribution of intensity from a single voxel among several components. The CLUMPFIND algorithm assigns emission from each voxel to one and only one clump. The advantages of CLUMPFIND are its simplicity and the fact that no a priori structure must be assumed for the clumps. Our method is more similar to the GAUSSCLUMPS algorithm presented by Stutzki & Güsten (1990) in that we assume a Gaussian profile for the clumps, and vary parameters to fit the observations, However, in the GAUSSCLUMPS algorithm, Gaussians are fitted to the observations on a one-by-one basis, with the second Gaussian fitted to the residuals after the first Gaussian has been subtracted from the data, etc. Our method differs in that all of the structures are fit to the data *simultaneously*; i.e., we construct a model from all of the Gaussian components and then fit that model to our observations. We believe that this results in a fairer competition between components for emission, albeit at a cost of greatly increased computation time and a frighteningly large parameter space to search.

[7] In finding the uncertainty for each parameter, we minimize χ^2 with respect to all other parameters; therefore, this uncertainty is conservative and represents the maximum possible deviation in each parameter which can produce a unity increase in the χ^2.

TABLE 1

PARAMETERS FOR GAUSSIAN COMPONENTS DERIVED FROM CUBE DECOMPOSITION

Component	Amplitude (10^{14} cm^{-2} [km s^{-1}]$^{-1}$)	Position		V_{LSR} (km s^{-1})	Δv_{obs} (km s^{-1})	Major Axis (arcsec)	Minor Axis (arcsec)	Position Angle (degrees)
		R.A. (arcsec)	Decl. (arcsec)					
1	4.5(8)	−60(15)	92(12)	7.20(3)	0.47(8)	171(35)	162(41)	70(23)
2	8.9(8)	−71(12)	4(9)	6.91(3)	0.33(4)	135(12)	106(12)	66(7)
3	13.6(4)	26(12)	−35(5)	6.65(2)	0.34(2)	195(9)	192(10)	11(6)
4	14.7(4)	−92(5)	−114(5)	6.47(2)	0.36(4)	206(15)	106(12)	56(3)
5	7.9(4)	−2(2)	17(12)	6.25(2)	0.40(2)	254(9)	211(15)	90(3)
6	11.7(4)	114(4)	102(11)	6.01(3)	0.50(4)	200(12)	144(20)	21(6)
7	14.0(4)	−43(8)	144(9)	5.79(1)	0.34(2)	186(10)	130(9)	−44(9)
8	6.6(6)	20(12)	2(14)	5.97(4)	0.27(1)	65(12)	62(12)	90(0)
9	7.9(4)	116(5)	−102(8)	6.76(4)	0.56(8)	121(15)	103(9)	0(7)

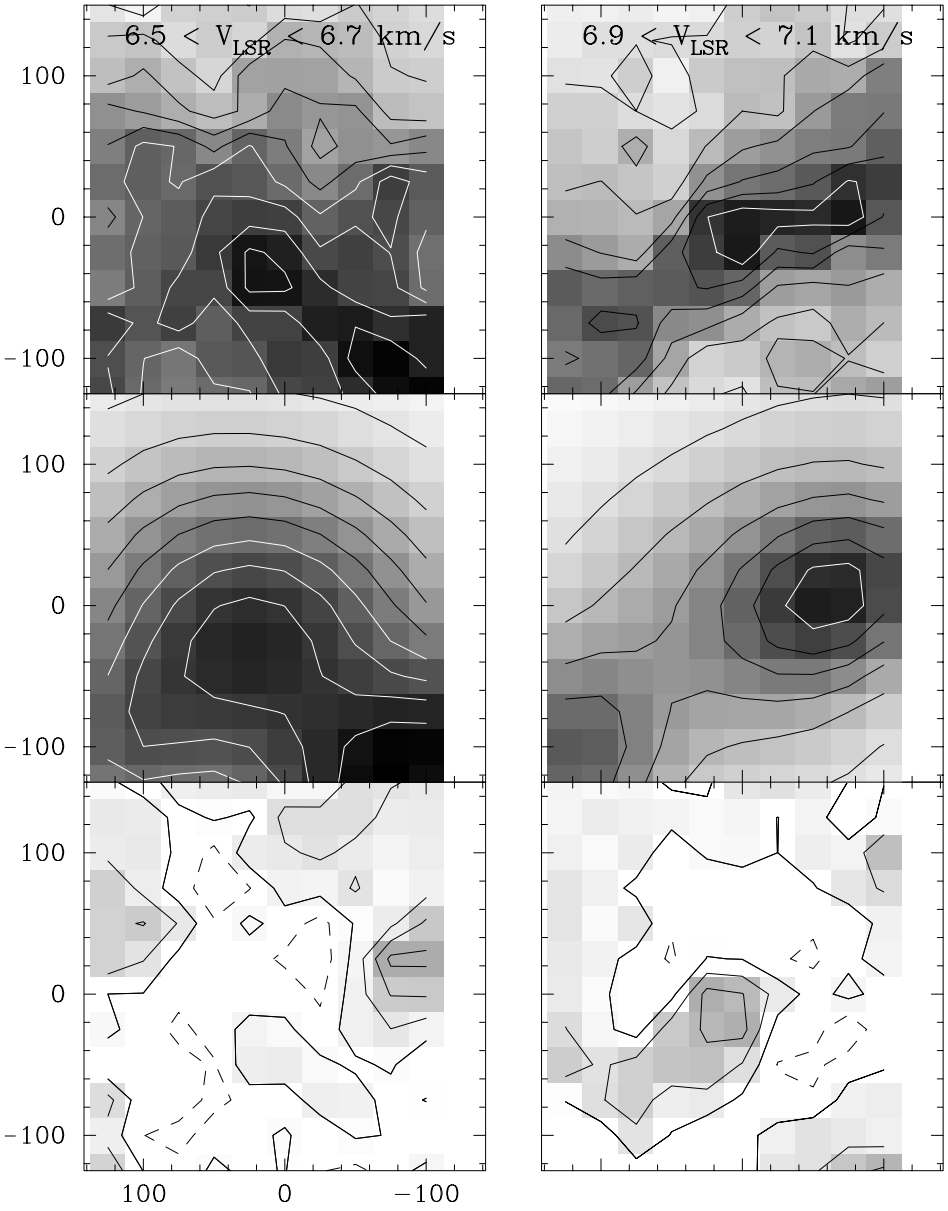

FIG. 5.—Comparison between $C^{18}O$ spectral column density (*top panels*) and nine-component model output (*middle panels*) integrated over two 0.2 km s^{-1} wide velocity ranges. The bottom panels show the residuals (i.e., data minus model). Coordinates on the lower left-hand panel indicate offset in arcseconds from the (0, 0) position of $04^h18^m6.9^s$, 26°54′54″ (1950) and apply to all panels. Contours in all panels increment by 3.8×10^{13} cm^{-2} (km s^{-1})$^{-1}$, and negative contours are plotted with dashed lines. White contours begin at 2.3×10^{14} cm^{-2} (km s^{-1})$^{-1}$.

range $5.75 < V_{LSR} < 7.25$ km s^{-1}, well within the 4.8–8.0 km s^{-1} range of the spectral column density cube.

In the following sections, we calculate physical properties of these clumps from the fitted parameters. These properties, along with the uncertainties determined from a propagation of the fitted parameter uncertainties, are given in Table 2.

3.3.1. *Size*

The typical clump has a fitted FWHM size 170″ × 135″. If we remove the broadening effects of the telescope beam (FWHM = 48″) by subtraction in quadrature, the average clump FWHM size is reduced to 162″ × 124″, or 0.11 × 0.09 pc for a distance of 145 pc. This size is similar to the sizes of dense star-forming cores, as measured by dense gas tracers such as NH_3 (Jijina, Myers, & Adams 1999) and HC_3N (Fuller & Myers 1993), and considerably smaller than the sizes typically found for $C^{18}O$ cores in Taurus (e.g., Onishi et al. 1996). Plotted in Table 2 is the geometric mean of the deconvolved FWHM major and minor axes for each clump.

The smallest clump (clump 8), with a deconvolved size of only 40″, is just barely resolved with our observations, while the largest has a FWHM size of 220″ and is comparable in size to the mapped area. Though the resolution and field of view of the observations yield this data set insensitive to smaller and larger structures, it is worthwhile to note that all of the observed emission can be accounted for with clumps whose sizes fall into this limited range.

3.3.2. *Velocity Dispersion*

The mean FWHM line width of the clumps is 0.38 km s^{-1}, with a maximum of 0.50 km s^{-1} and a minimum of 0.27 km s^{-1}. Once again, these values are more similar to

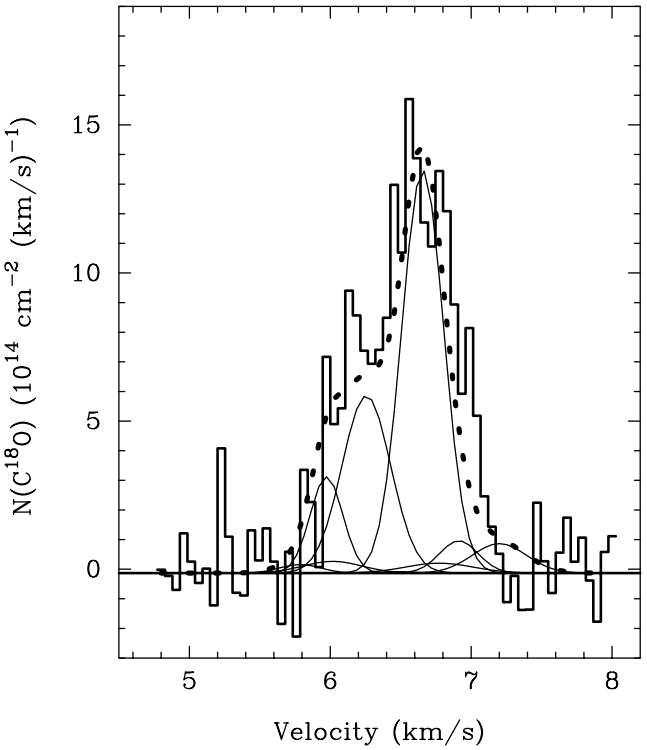

FIG. 6.—Comparison between the $C^{18}O$ spectral column density data (*histogram*) and the nine-component model output (*solid line*) as a function of velocity for emission toward the (−25″, −25″) position. The model output contains the contributions from several Gaussian components which overlap at this position. The contributions from each individual component are indicated by the thin solid lines. This particular spectrum is dominated by emission from two components.

the line widths found with dense gas tracers than those more commonly associated with CO emission.

A gas of molecules of molecular weight 30 amu (i.e., $C^{18}O$) at a temperature of 10 K, whose motions are purely thermal, will emit lines whose line width is 0.12 km s^{-1}. The nonthermal line width of the observed emission can then be found by quadrature subtraction of the observed line width and the thermal line width. Since the line widths of the clumps are significantly greater than the thermal line width of 10 K $C^{18}O$, the nonthermal line width is essentially equal to the observed line width.

However, in a 10 K gas the thermal velocity of molecules of molecular weight 2.3 amu (the mean molecular weight of molecules in cloud material) is much higher and would produce a line width of 0.45 km s^{-1}, if these molecules were to emit. It is this larger thermal line width that is indicative of the thermal kinetic energy content of the cloud. Thus the ratio of thermal to nonthermal kinetic energy in these clumps is greater than or nearly equal to one, and many of the clumps are dominated by thermal motions.

Thermally dominated emission has generally been seen with tracers that select only the highest density material in dense cloud cores (e.g., Benson & Myers 1989; Fuller & Myers 1993). However, our $C^{18}O$ observations indicate that thermally dominated clumps may be present throughout dark clouds, even at locations with lower densities.

Plotted in Table 2 is the inferred total line width for a gas of molecule of mass 2.3 amu for each clump. This line width consists of the quadrature addition of the 10 K thermal line width and the nonthermal line width found from our $C^{18}O$ data. The mean value for the nine clumps is 0.58 km s^{-1}, or 1.3 times the 10 K thermal line width.

3.3.3. *Column Densities and Clump Masses*

Though the peak spectral column density in velocity-resolved units is the fitted quantity, the velocity-integrated column density for each clump is more physically interesting. The average $C^{18}O$ column density is 4.1×10^{14} cm^{-2}, which converts to a molecular hydrogen column density of 3.6×10^{21} cm^{-2} using the prescription of Frerking et al. (1982). Thus the average column density for a single clump is roughly half of the map-averaged column density determined from the total integrated intensity above. The peak H_2 column densities are listed in Table 2.

A crude estimate for the mean volume density of each clump can be obtained by dividing the peak column density by the deconvolved FWHM clump size. This yields an average density of 1.2×10^4 cm^{-3} for the nine clumps, whose individual values range from 6.5×10^3 cm^{-3} to 2.6×10^4 cm^{-3}. These densities are typical for star-forming core material and higher than that generically found in CO-emitting regions.

The mass of each clump can be determined by integrating the column density distribution over both spatial dimensions. The derived clump masses listed in Table 2 range from 0.03 to 1.7 $M_\odot$, with an average mass of 0.9 $M_\odot$. The sum of the masses of all of the clumps (7.8 $M_\odot$) is approximately twice the mass determined from the $C^{18}O$ integrated intensity above (4.2 $M_\odot$). There are two reasons for this discrepancy. First, though the centers of all clumps are within the mapped area, substantial portions of some clumps extend beyond the edges of our map. Thus, the total

TABLE 2

CLUMP PROPERTIES

Component	N (H_2) (10^{20} cm^{-2})	FWHM Size (pc)	Density (10^3 cm^{-3})	Mass ($M_\odot$)	Δv_{H_2} (km s^{-1})	α
1	25(2)	0.11(2)	7(1)	0.7(2)	0.63(6)	7(3)
2	30(2)	0.08(1)	13(1)	0.37(6)	0.54(2)	6(1)
3	41(1)	0.13(1)	10.0(4)	1.5(1)	0.54(1)	2.8(3)
4	45(1)	0.10(1)	15(1)	0.88(9)	0.56(2)	3.6(5)
5	32(1)	0.16(1)	6.5(3)	1.7(1)	0.58(1)	3.4(3)
6	48(1)	0.11(1)	14(1)	1.3(2)	0.66(3)	3.9(7)
7	42(1)	0.10(1)	13.0(6)	0.93(7)	0.54(1)	3.4(3)
8	23(1)	0.03(1)	26(8)	0.04(4)	0.50(1)	19(12)
9	40(1)	0.07(1)	18(2)	0.41(7)	0.70(6)	9(2)

mass of some clumps includes substantial contributions from material outside of the mapped area. Second, the Frerking et al. (1982) conversion from $N(C^{18}O)$ to $N(H_2)$ includes a constant value in addition to a linear term. The "extra" column density due to this constant term has been added to each of the clumps, and so along some lines of sight that contain more than one clump, we may have overestimated the contribution from this constant term.

3.4. *Comparison with Dense Gas and Forming Stars*

HC_3N $J = 4$–3 observations were made toward selected positions to examine the velocity structure of the dense gas in this region. Because it has a higher dipole moment (3.6 D), HC_3N is significantly excited only in zones of high volume density ($n > 10^5$ cm^{-3}). $J = 4$–3 emission has been detected toward many starless and star-forming cores in the Taurus molecular cloud and elsewhere (Fuller & Myers 1993).

Unlike the $C^{18}O$ emission, all HC_3N spectra are well fitted by a single Gaussian velocity component. The spectra toward the northern and southern infrared sources in this region[8] are shown in the top panels of Figures 7 and 8, along with single Gaussian component fits. Note that the appearance of the HC_3N spectra is complicated by the hyperfine splitting of the $J = 4$–3 transition; while three spectral features are present (the two lower velocity features are blended), these features result from the splitting of the upper and lower levels of the transition and not from the velocity structure of material along the line of sight.

The inferred velocity distributions at both positions have very narrow line widths that are considerably smaller than the thermal line width of H_2 at 10 K. Therefore, the dense gas traced by the HC_3N $J = 4$–3 emission is dominated by thermal motions. The narrow line widths also demonstrate that much of the material detected in $C^{18}O$ is not sufficiently dense to excite HC_3N emission, since the $C^{18}O$ emission extends over a far broader velocity range. The bottom panels of Figures 7 and 8 show the $C^{18}O$ emission toward the northern and southern young stars, respectively, along with a Gaussian that indicates the line center velocity and line width of the HC_3N-emitting material.

Toward the southern source (Fig. 7), the $C^{18}O$ spectrum peak is coincident in velocity with the HC_3N line center, and the velocity distribution of the emission in both tracers is similar, except for an excess of low-velocity $C^{18}O$ emission. Toward the northern source (Fig. 8), however, there is less correspondence between the HC_3N and $C^{18}O$ velocity structure. Once again, the $C^{18}O$ spectrum peaks at the line center velocity of the HC_3N emission, but toward this source, there is a substantial amount of low-velocity $C^{18}O$ emission that does not emit HC_3N.

While the HC_3N emission does not match well with the total $C^{18}O$ emission toward these sources, it does match well, in both line center velocity and line width, with two of the clumps identified in our decomposition of the $C^{18}O$ emission. The HC_3N emission toward the northern infrared source has line center and line width consistent with clump 2, the center of which is 18″ to the southwest. Likewise the line center and line width of the HC_3N emission toward the southern source are consistent with clump 3, the center of which is 34″ to the east.

This correspondence in position, velocity, and line width indicates that the HC_3N emission originates from dense material in clumps 2 and 3. If this dense material is associated with the two forming stars in the region, then clumps 2 and 3 may comprise the reservoirs out of which these stars formed. Additional observations made at selected positions within the $C^{18}O$-mapped region tend to support this possibility. Toward all positions where HC_3N emission was detected, the velocity structure could be fitted with a single Gaussian with line width less than 0.50 km s^{-1}. Furthermore, the line center velocities of detections in the northwestern portion of the mapped area were consistent with the line center velocity of clump 2, and the line center

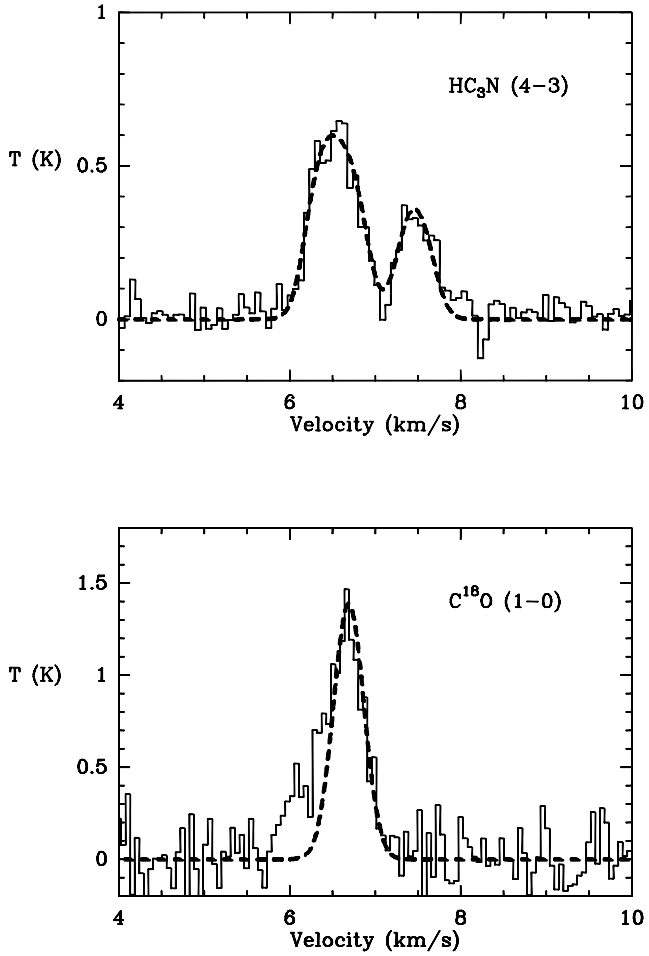

FIG. 7.—Antenna temperature (T_A^*) as a function of velocity in the HC_3N $J = 4$–3 line toward the southern near-infrared source in the I04181 region (*top panel*). The position observed is R.A. $4^h18^m6^s.3$ and decl. 26°54′8″ (1950), or an offset of (−8″, −46″) from the (0, 0) position defined in Fig. 1. Emissions from three hyperfine transitions are present in the spectrum. The dotted line indicates the best fit to the hyperfine structure using a single Gaussian velocity structure. The fitted Gaussian has an LSR line center velocity of 6.65 km s^{-1}, and a FWHM line width of 0.42 km s^{-1}. The $C^{18}O$ spectrum toward this position is shown (*bottom panel*), along with a Gaussian (*dotted line*) reflecting the line center velocity and line width of the HC_3N $J = 4$–3 emission. The amplitude of the Gaussian is adjusted to match the $C^{18}O$ line intensity roughly.

[8] We do not present observations toward the middle near-infrared source because new analysis of the continuum emission from this source suggests that it is not a deeply embedded source, but rather a more evolved class II source located on the far side of the cloud and whose spectrum is extinguished by the intervening cloud material (R. F. Ladd & A. C. Schwortz, in preparation). Though HC_3N $J = 4$–3 emission (and therefore dense gas) was detected along this line of sight, its line center velocity and line width suggest that it arises from material associated with the southern class I source.

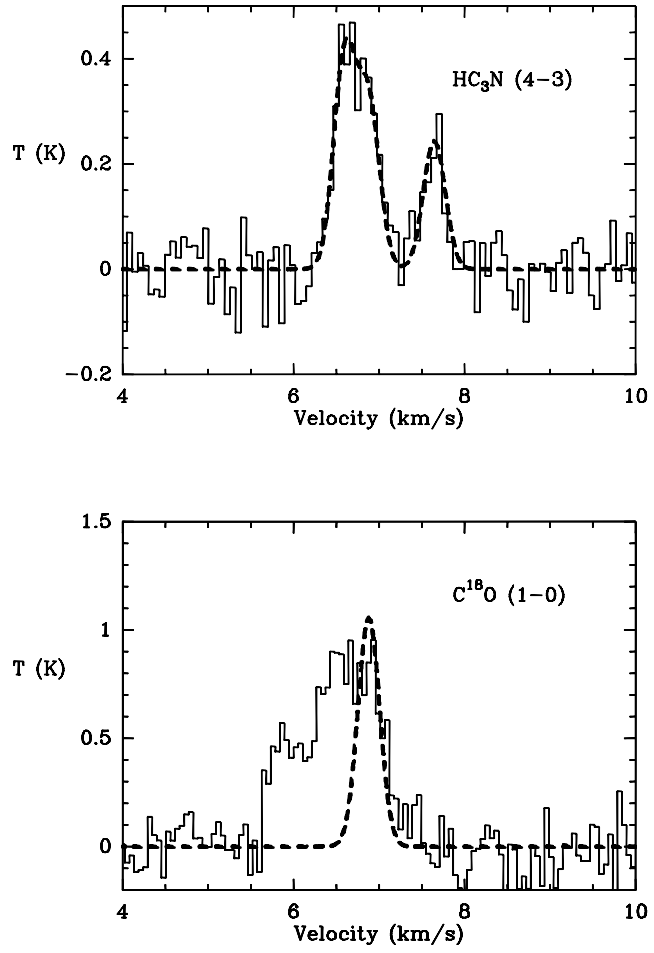

FIG. 8.—Antenna temperature (T_A^*) as a function of velocity in the HC_3N $J = 4$–3 line toward the northern near-infrared source in the I04181 region (*top panel*). The position observed is R.A. $4^h18^m2.9^s$ and decl. 26° 55′15″ (1950), or an offset of (−53″, +21″) from the (0,0) position defined in Fig. 1. Emissions from three hyperfine transitions are present in the spectrum. The dotted line indicates the best fit to the hyperfine structure using a single Gaussian velocity structure. The fitted Gaussian has an LSR line center velocity of 6.91 km s^{-1}, and a FWHM line width of 0.30 km s^{-1}. The $C^{18}O$ spectrum toward this position is shown (*bottom panel*), along with a Gaussian (*dotted line*) reflecting the line center velocity and line width of the HC_3N $J = 4$–3 emission. The amplitude of the Gaussian is arbitrary.

velocities of detections in the middle and southern portions of the map were consistent with the line center velocity of clump 3. Toward the extreme southeast, strong HC_3N emission with a line center velocity of 6.68 km s^{-1} was detected; this velocity is consistent with the line center velocity of both clumps 3 and 9, and given the position of this strong emission near the center of clump 9, we speculate that clump 9 may also harbor dense gas. There is no evidence that any of the other clumps identified in the $C^{18}O$ decomposition contain dense gas.

4. DISCUSSION

4.1. *The Reality of These Clumps*

There are many ways to characterize the emission from molecular clouds and to infer the structure that might be responsible for the emission. Many methods use a global approach and concentrate on the structure as a function of size scale and velocity separation (e.g., Miesch & Bally 1994; Heyer & Schloerb 1997). The output of such efforts are typically scaling laws, which describe how a cloud behaves over a range of size scales, rather than delineating a specific point-by-point structure. One of the first major results to come from this type of analysis was the discovery of Larson's laws (Larson 1981), which relate size scale and velocity dispersion over a wide range in sizes scales.

Global methods are particularly useful for large-scale regimes in which turbulence may play a dominant role in structuring the medium. Indeed, many authors have suggested that the self-similarity and scale-free structure implied by Larson's laws can be understood as a product of turbulent energy input (e.g., Goodman et al. 1998)

The method used in this work adopts a different approach, assuming instead that the medium consists of a collection individual structures, each with definable properties such as mass, size, etc. This approach has been used many times to identify the "clump structure" of cloud material ranging from giant molecular clouds (e.g., Blitz & Stark 1986; Carr 1987; Stutzki & Güsten 1990; Williams, de Geus, & Blitz 1994; Kramer et al. 1998) to substellar mass knots in dark clouds (e.g., Heithausen et al. 1998) and dense cores (e.g., Langer et al. 1995; Peng et al. 1998).

The assumption that clumps of gas exist within dark cloud material is better supported on smaller scales, since we know that such structures exist in star-forming regions. If stars are to form, coherent structures of roughly stellar mass must be present and (probably) gravitationally unstable to collapse. In regions that form low-mass stars, these structures have been documented with observations of dense gas tracers, and their presence as well-defined entities within dark clouds is established (e.g., Benson & Myers 1989). Our limited HC_3N observations indicate that narrow line width thermally dominated dense gas is present in this region as well.

Thus it is reasonable to presume that solar mass–sized structures might be found in the I04181 region. At least two and possibly three stars have recently formed from this material, and their presence as class I/II sources shows that this environment has recently been receptive to the formation of bound clumps of solar mass size. Furthermore, the structure of the observed $C^{18}O$ emission indicates qualitatively the presence of such structures. The line profiles in Figure 2 are readily interpreted as superpositions of structures with line widths in the "thermally dominated" (i.e., $0.12 < \Delta v < 0.5$ km s^{-1}) range, and the channel maps of Figure 3 show overlapping structures whose size, when coupled with a density of 10^4 cm^{-3}, yield masses near 1 $M_\odot$. The presence of HC_3N emission with properties (e.g., line center velocity and line width) very similar to those of several clumps identified independently in $C^{18}O$ lends further credence to our decomposition of the $C^{18}O$-emitting material.

Nonetheless, since we began with a presumption that the emission was structured into clumps, we cannot claim that our result proves their existence. However, we can say, based on our fitting algorithm, that if the emission from the I04181 region can be characterized by clumplike emission, then the following are true:

1. *The number of clumps required to model the spatial and velocity structure observed adequately is small, and the model so constructed fits the data well.* The multipeaked line profiles in the spectra of Figure 2 provide strong support for this statement. If a large number of structures were present

and had uncorrelated line center velocities, the observed spectra would appear smooth over the entire velocity interval (e.g., Tauber, Goldsmith, & Dickman 1991). The presence of a few distinct peaks in each spectrum indicates that a small number of structures are responsible for the emission along each line of sight. Furthermore, comparisons between adjacent and nearby spectra indicate that structures identified by a peak in a given spectrum are spatially persistent and extend over regions considerably larger than the telescope's FWHM beam size. Additional structures of smaller size and lower column density may be present in the cloud, but they are not identified owing to beam size and sensitivity limitations of the observations. However, since they contribute little or no detected emission, these unseen structures must contain only a very small fraction of the region's molecular mass.

2. *The clumps identified in this region have mean size* 0.1 pc, *line width* 0.35 km s^{-1}, *and mass of* 1 $M_\odot$, *all of which are consistent with the structures expected in low-mass star-forming regions.* These parameters are determined from our multicomponent decomposition of the observed data cube, but it is obvious even from visual examination of Figures 2 and 3 that the data will be best fitted by line widths and sizes close to these values.

3. *There is no obvious need for a large-scale* "interclump" *or background component, nor are there a small number of bright clumps whose size is smaller than the resolution of the observations.* There is no single structure that appears in every spectrum at the same intensity; however, clump 5 has a FWHM size that is comparable to the mapped area, so it is possible that the emission associated with this "clump" is in fact part of a larger background component. If so, then this background component has a line width comparable to that of the other clumps in the region and even this large-scale background emission is thermally dominated (however, see § 4.2.2 below).

4. *If substructure exists within any of the defined clumps, the dispersion in the velocities of such substructures must be small compared to the thermal line width of a molecule of mean molecular mass* (*e.g.*, 0.5 km s^{-1}). The clumps identified in this work are distinct entities within our (x, y, v) data cube, but they could result from the superposition of a number of smaller structures within the cloud. If so, however, then these substructures are constrained to have nearly common line center velocities and must be arranged spatially such that their superposition along our line of sight mimics a smooth, centrally peaked structure. This last criterion is difficult to satisfy unless we occupy a special location with respect to the cloud, or the substructures are all colocated in space. However, if the substructures are colocated in space and have nearly similar line center velocities, then it is difficult to see how they can be distinguished from one another, and their identity as distinct substructures is suspect. Interferometric examination of similar thermally dominated cores show that at most 10% of the observed emission arises from smaller structures (Langer et al. 1995).

4.2. *The Stability of the Clumps*

4.2.1. *Virial Parameters*

The stability of a given clump can be estimated from its virial parameter α, which is essentially the ratio of kinetic to gravitational energy for a structure (Bertholdi & McKee 1992):

$$\alpha = \frac{5R\sigma^2}{GM},$$

where R is the clump radius (assumed half of the FWHM size), σ is the velocity dispersion of material of mean molecular mass, G is Newton's constant of gravitation, and M is the clump mass. Values of α for each clump are listed in Table 2, along with propagated uncertainties. The mean value for the nine clumps is 5.8, and all have $\alpha > 1.0$, indicating that none are formally unstable to gravitationally induced collapse.

However, the five most massive clumps have low values of α (~ 3), and it is clear that in these clumps gravity plays a substantial role in the dynamics. Given the large uncertainties in α *and* the additional uncertainty in the conversion from $N(C^{18}O)$ to $N(H_2)$, it is entirely plausible that these clumps are gravitationally bound and susceptible to collapse. In addition, an external pressure from overlying layers of molecular cloud material may exert an additional confining influence.

4.2.2. *Estimating an External Pressure*

We can estimate the properties required of an external medium if it is to pressure confine the clumps with $\alpha = 3$, as follows:

$$n_{\rm ext}\,\sigma_{\rm ext}^2 = \left(1 - \frac{1}{\alpha}\right) n_{\rm clump}\,\sigma_{\rm clump}^2,$$

where $n_{\rm ext}$ and $n_{\rm clump}$ are the volume densities of the external medium and clump, respectively, and $\sigma_{\rm ext}$ and $\sigma_{\rm clump}$ are the velocity dispersions of the external medium and clump, respectively. This expression is a modified form of that presented by Peng et al. (1998).

For $n_{\rm clump} = 10^4$ cm^{-3}, $\sigma_{\rm clump} = 0.25$ km s^{-1}, and $\alpha = 3$, $n_{\rm ext}\,\sigma_{\rm ext}^2 = 420$ cm^{-3} (km s^{-1})^2. It is difficult to estimate the properties of the confining medium, since our observations are apparently insensitive to it. However, one estimate of its nonthermal velocity dispersion comes from the dispersion in the line center velocities of the clumps themselves (i.e., the "clump-to-clump" velocity dispersion), which is 0.48 km s^{-1}. Here we assume that the clumps are embedded in the larger medium and that their motions are characteristic of the macroscopic streaming motions within this medium. Combining this value in quadrature with the thermal velocity dispersion of a molecule of mean mass with a temperature of 10 K, we get a total velocity dispersion of 0.51 km s^{-1}. Using this value and the above relation, we require an external density of 1.5×10^3 cm^{-3} to confine the $\alpha = 3$ clumps.

A density this high is a bit problematic, since it is comparable to the critical density for the $C^{18}O$ $J = 1$–0 transition, and therefore, we might expect to see emission from this component if present. However, our choice of velocity dispersion is really the minimum acceptable value, since the velocity dispersion of an external enveloping medium would have to be at least as large as the velocity dispersion of the clumps it envelops. With a velocity dispersion only 30% larger than this value, a confining medium can have a density less than 10^3 cm^{-3}. Thus it appears likely that the $\alpha = 3$ clumps can be externally confined and will have life-

times considerably longer than their crossing times ($\sim 2 \times 10^5$ yr).

As has been noted above, it is possible that the emission ascribed to clump 5 is in fact this interclump medium. If so, then the velocity dispersion ($\sigma = 0.25$ km s^{-1}) and inferred volume density ($n \sim 6 \times 10^3$ cm^{-3}) are sufficient to provide the confining pressure for the other $\alpha = 3$ clumps. However, the clump 5 emission is distributed over a velocity range small compared to the clump-to-clump velocity dispersion, so it is difficult to see how this material could provide an isotropic confining pressure to clumps with very different line center velocities. Based on its narrow line width, we consider it unlikely that the clump 5 emission represents the interclump medium.

4.3. *Implications for Cloud Structure in and near Dense Cores*

Our successful decomposition of the molecular gas emission in the I04181 region into a small number of distinct thermally dominated dense clumps challenges the traditional notion of a dense core as the only quiescent region in an otherwise turbulent medium (e.g., Goodman et al. 1998). Instead, for at least this region, we replace this paradigm with that of a collection of quiescent entities that comprise nearly all of the mass in the region and that exist with little or no interclump medium. The larger line widths seen on larger scales and with higher optical depth lines are then a measure of the clump-to-clump motions.

This idea is not at all new in its general presentation. Clumpy cloud models have been invoked for more 20 years to explain the characteristics of molecular clouds including line profiles and radiative transfer through cloud material (e.g., Zuckerman & Evans 1974; Martin, Sanders, & Hills 1984), the presence of dissociating and ionizing ultraviolet radiation deep within clouds (e.g., Stutzki et al. 1988; Schilke et al. 1995; Plume et al. 1999), and the lack of self-similarity in cloud structure at small (i.e., 0.1 pc) scales (e.g., Blitz & Williams 1997).

Our analysis indicates that nearly all of the mass in the I04181 region is concentrated into a small number of relatively large clumps. This result is consistent with many cloud decomposition efforts, which quite generally show that, while the greatest number of clumps are of very small size, the bulk of a cloud's mass is concentrated into a small number of the largest clumps (e.g., Kramer et al. 1998).

The new result from our study is that the molecular cloud "building blocks" in the I04181 region are comparable in size and mass to star-forming cores and have narrow line widths. This implies that the local environment for most of the material in the cloud is dominated by thermal motions and that the broad line widths seen with more opaque lines of more abundant tracers result from the superposition of many of these clumps.

The size scale we find for these quiescent clumps, 0.1 pc, has been identified as an important scale for core formation by a variety of authors for a variety of reasons. Benson & Myers (1989) first showed this to be the typical size dense cores in NH_3 and showed that for a density of $\sim 10^4$ cm^{-3}, a core of this size contains roughly a solar mass of material. Goodman et al. (1998) show that size–line width relations, which apply for cloud measurements on larger scales, break down at 0.1 pc scales and that at smaller scales, the line width is independent of (or at most, weakly dependent on) size scale. Last, Larson (1995) has shown that the typical young star in Taurus has a companion located within 0.05 pc and that this size scale defines a transition between binary and more multiply clustered regimes.

Identification of these structures in the I04181 region has been facilitated by the large dispersion in line center velocities of the clumps, so that clumps overlapping in the two available spatial dimensions are still distinct in the velocity dimension. Cursory examination of the emission from other dense core regions in Taurus indicates that this situation is somewhat unusual and that $C^{18}O$ spectra with distinct multiple peaks extending over ~ 2 km s^{-1} are relatively rare. Nonetheless, the typical $C^{18}O$ spectrum is decidedly non-Gaussian and might result from a superposition of quiescent clumps with a smaller clump-to-clump dispersion. Efforts are currently underway to test this hypothesis in other dense core regions.

The large size of these structures in dense cores initially appears inconsistent with the results of Falgarone, Phillips, & Walker (1991), Falgarone et al. (1998), and others who observe structure on very small scales in some clouds. However, regions where the small or unresolved structure is found are preferentially located on the edges (in either space or velocity) of the cloud material and not in the densest portion of the cloud. In those highly structured regions, gas velocities indicate the presence of large accelerations (Falgarone et al. 1998), and it appears that turbulent processes may dominate the dynamics.

The change in physical properties from a turbulent medium of low volume-averaged density to a quiescent region of higher density has been dubbed the "transition to coherence" by Goodman et al. (1998), who speculate that a decrease in fractional ionization or a steep increase in density prevent the injection of turbulent magnetic energy into the densest material. Our results suggest that this transition to coherence may take place not just once or twice, but quite often within the hearts of molecular clouds, and that thermally dominated structures may be common in dense regions. Since we see only a few of these structures in HC_3N emission, we conclude that many of them do not reach (or have not yet reached) densities high enough to be anointed as "dense cores." Dense gas observations throughout Taurus generally detect only one structure in each dense region, so if these regions are populated with a number of quiescent structures, the ones dense enough to be detectable in NH_3 or HC_3N are relatively rare.

This view of the dense regions of clouds is unifying in that it explains the observations of dense gas as well as lower density molecular material with a single physical picture. Tracers of dense gas (e.g., HC_3N, NH_3) detect the densest of the collection of quiescent structures in the region, and these observations have narrow, thermally dominated line widths. Observations with tracers sensitive to lower densities (e.g., $C^{18}O$) detect several clumps along each line of sight, resulting in emission distributed over a broader range in velocity and space.

The presence of a number of quiescent clumps in each dense region can naturally explain why the mass of a $C^{18}O$ "core" (that is, one identified from integrated intensity maps; e.g., Onishi et al. 1996) is so much larger than the mass of the star it forms, since only one clump is involved in the star formation event, and the others are merely bystanders. Moreover, the presence of a number of quiescent clumps in a region increases the chance that more than one clump is instable to collapse and may provide an explana-

tion for coeval star formation and small-scale clustering (e.g., Chen & Tokunaga 1994; Hodapp & Ladd 1995).

5. CONCLUSIONS

1. We present $C^{18}O$ $J = 1$–0 observations of the I04181 star-forming region. In a 0.18 × 0.21 pc area, we detect 4.2 $M_\odot$ of molecular material.

2. The spectra indicate the presence of several distinct clumps along many lines of sight, and channel maps show that this emission is generated by a small number of distinct, but spatially overlapping structures.

3. We have modeled the three-dimensional (two space dimensions and one velocity dimension) distribution of column density in this region with nine Gaussian structures whose positions, sizes, line widths, and spatial aspect ratios are free parameters. All of the observed emission can be accounted for with a model containing nine Gaussian structures and no interclump medium. This best-fit model has a reduced χ^2 of 1.55.

4. The nine clumps defined with the decomposition process have a mean FWHM size of 0.1 pc, mean $C^{18}O$ column density of 4.1×10^{14} cm^{-2}, and a mean mass of 0.9 $M_\odot$. All of the clumps have nonthermal line width less than or equal to the thermal line width of molecular hydrogen at a temperature 10 K, and therefore these clumps are dominated by thermal motions.

5. In contrast to the $C^{18}O$ observations, HC_3N $J = 4$–3 observations of the same region show emission from only one Gaussian structure along each measured line of sight. The line center velocities and line widths of the HC_3N emission correspond well to those of two or possibly three $C^{18}O$ clumps in the region and indicate that only a subset of the $C^{18}O$-detected clumps harbor high-density material.

6. The ratio of gravitational to kinetic energy indicates that none of these clumps is unstable to collapse from gravitational forces alone; however, for several of clumps, the combination of self-gravity and reasonable estimates of external pressure may be sufficient for stability. Thus, at least a few clumps are likely long-lived and may be susceptible to collapse and star formation. By combining the HC_3N and $C^{18}O$ data, we identify two specific clumps as the reservoirs from which the class I sources in the region have recently formed.

We thank Chris deVries for his assistance in adapting the differential evolution algorithm for analysis of astronomical data. We also thank our referee, Jürgen Stutzki, for valuable comments on our manuscript. E. F. L. acknowledges the generous support of the University of Manchester Institute of Science and Technology during the preparation of this work. K. R. C. acknowledges the support of the Bucknell University Research Experiences for Undergraduates (REU) program funded by the National Science Foundation (NSF-PH9732158).

REFERENCES

Barnard, E. E. 1927, Atlas of Selected Regions of the Milky Way, ed. E. B. Frost & M. M. Calvet (Washington, DC: Carnegie Institution of Washington)
Benson, P. J., & Myers, P. C. 1989, ApJS, 71, 89
Bergin, E. A., & Langer, W. D. 1997, ApJ, 486, 316
Bertoldi, F., & McKee, C. F. 1992, ApJ, 395, 140
Blitz, L., & Stark, A. A. 1986, ApJ, 300, L89
Blitz, L., & Williams, J. P. 1997, ApJ, 488, L145
Carr, J. S. 1987, ApJ, 323, 170
Chen, H., & Tokunaga, A. T. 1994, ApJS, 90, 149
Erickson, N. R., Goldsmith, P. F., Novak, G., Grosslein, R. M., Viscuso, P. J., Erickson, R. B., & Predmore, C. R. 1992, IEEE Trans. Micro. Theory Tech., 40, 1
Falgarone, E., Panis, J.-F., Heithausen, A., Perault, M., Stutzki, J., Puget, J.-L., & Bensch, F. 1998, A&A, 331, 669
Falgarone, E., Phillips, T. G., & Walker, C. K. 1991, ApJ, 378, 186
Frerking, M. A., Langer, W. D., & Wilson, R. W. 1982, ApJ, 262, 590
Fuller, G. A., & Myers, P. C. 1993, ApJ, 418, 275
Gaida, M., Ungerechts, H., & Winnewisser, G. 1984, A&A, 137, 17
Goodman, A. A., Barranco, J. A., Wilner, D. J., & Heyer, M. H. 1998, ApJ, 504, 223
Heithausen, A., Bensch, F., Stutzki, J., Falgarone, E., & Panis, J. F. 1998, A&A, 331, L65
Heyer, M. H., & Schloerb, F. P. 1997, ApJ, 475, 173
Hodapp, K.-W., & Ladd, E. F. 1995, ApJ, 463, 97
Hogerheijde, M. R., Van Dishoeck, E. F., Blake, G. A., & Van Langevelde, H. J. 1997, ApJ, 489, 293
Jijina, J., Myers, P. C., & Adams, F. C. 1999, ApJS, 125, 161
Juvela, M., Lehtinen, K., Mattila, K., Lemke, D., & Haikala, L. 1997, A&A, 317, 898
Kenyon, S. J., Dobrzycka, D., & Hartmann, L. 1994, AJ, 108, 1872
Kenyon, S. J., Whitney, B. A., Gomez, M., & Hartmann, L. 1993, ApJ, 414, 773
Kramer, C., Stutzki, J., Röhrig, R., & Corneliussen, U. 1998, A&A, 329, 249
Kutner, M. L., & Ulich, B. L. 1981, ApJ, 250, 341
Langer, W. D., Velusamy, T., Kuiper, T. B. H., Levin, S., Olsen, E., & Migenes, V. 1995, ApJ, 453, 293
Lada, C. J., Lada, E. A., Clemens, D. P., & Bally, J. 1994, ApJ, 429, 694
Ladd, E. F., & Heyer, M. H. 1996, FCRAO Technical Memorandum, Univ. of Massachusetts
Larson, R. B. 1981, MNRAS, 194, 809
———. 1995, MNRAS, 272, 213
Lynds, B. T. 1962, ApJS, 7, 1
Martin, H. M., Sanders, D. B., & Hills, R. E. 1984, MNRAS, 208, 35
Miesch, M., & Bally, J. 1994, ApJ, 429, 645
Moriarty-Schieven, G. H., Wannier, P. G., Mangum, J. G., Tamura, M., & Olmsted, V. K. 1995, ApJ, 455, 190
Onishi, T., Mizuno, A., Kawamura, A., Ogawa, H., & Fukui, Y. 1996, ApJ, 465, 815
Peng, R., Langer, W. D., Velusamy, T., Kuiper, T. B. H., & Levin, S. 1998, ApJ, 497, 842
Plume, R., Jaffe, D. T., Tatematsu, K., Evans, N. J., II., & Keene, J. 1999, ApJ, 512, 768
Preibisch, T., & Smith, M. D. 1997, A&A, 322, 825
Price, K., & Storn, R. 1997, Dr. Dobb's J., 26(4), 18
Schilke, P., Keene, J., Le Bourlot, J., Pineau des Forets, G., & Roueff, E. 1995, ApJ, 294, L17
Stutzki, J., & Güsten, R. 1990, ApJ, 356, 513
Stutzki, J., Stacey, G. J., Genzel, R., Harris, A. I., Jaffe, D. T., & Lugten, J. B. 1988, ApJ, 332, 379
Tauber, J. A., Goldsmith, P. F., & Dickman, R. L. 1991, ApJ, 375, 635
Williams, J. P., deGeus, E. J., & Blitz, L. 1994, ApJ, 428, 693
Zuckerman, B., & Evans, N. J. 1974, ApJ, 192, L149